In-Vivo Electrical Properties Estimation of Biological Tissues by Means of a Multi-Step Microwave Tomography Approach

Michele Ambrosanio, *Member, IEEE*, Martina Teresa Bevacqua, *Member, IEEE*, Joe LoVetri, *Senior Member, IEEE*, Vito Pascazio, *Fellow, IEEE*, and Tommaso Isernia, *Fellow, IEEE*

***Abstract*— The accurate quantitative estimation of the electromagnetic properties of tissues can serve important diagnostic and therapeutic medical purposes. Quantitative microwave tomography is an imaging modality that can provide maps of the *in-vivo* electromagnetic properties of the imaged tissues, *i.e.* both the permittivity and the electric conductivity. A multi-step microwave tomography approach is proposed for the accurate retrieval of such spatial maps of biological tissues. The underlying idea behind the new imaging approach is to progressively add details to the maps in a step-wise fashion starting from single-frequency qualitative reconstructions. Multi-frequency microwave data is utilized strategically in the final stage. The approach results in improved accuracy of the reconstructions compared to inversion of the data in a single step. As a case study, the proposed workflow was tested on an experimental microwave data set collected for the imaging of the human forearm. The human forearm is a good test case as it contains several soft tissues as well as bone, exhibiting a wide range of values for the electrical properties.**

***Index Terms*— Quantitative microwave tomography, biomedical microwave imaging, tissues electric properties estimation, experimental medical imaging, electromagnetic inverse scattering.**

Manuscript received 30 November 2023; accepted 6 January 2024. Date of publication 15 January 2024; date of current version 2 May 2024. This work was supported in part by Piano Operativo Salute through the project "RADIOAMICA: Open network per la radiomica/radiogenomica cooperativa basata su intelligenza artificiale" under Grant CUP C33C22000380006; in part by local funding "Sustainable Change: Toward a Society of Inclusion, Health and Green Economy" financed by the University of Naples Parthenope; and in part by PRIN project DISCERN, Advanced Hybrid Breast Cancer Imaging under Grant CUP C53D23000430006. *(Michele Ambrosanio and Martina Teresa Bevacqua are co-first authors.) (Corresponding author: Martina Teresa Bevacqua.)*

This work involved human subjects or animals in its research. Approval of all ethical and experimental procedures and protocols was granted by the University of Manitoba Biomedical Research Ethics Board under Reference No. B2010:159.

Michele Ambrosanio is with the DiSEGIM, Department of Economics, Law, Cybersecurity, and Sports Sciences, University of Naples Parthenope, 80035 Naples, Italy (e-mail: michele.ambrosanio@uniparthenope.it).

Martina Teresa Bevacqua and Tommaso Isernia are with the Dipartimento di Ingegneria dell'Informazione, delle Infrastrutture e dell'Energia Sostenibile (DIIES), Università degli Studi Mediterranea di Reggio Calabria, 89124 Reggio Calabria, Italy, also with the Inter-University National Research Center on Interactions between Electromagnetic Fields and Biosystems (ICEmB), 16145 Genoa, Italy, and also with the Consorzio Nazionale Interuniversitario per le Telecomunicazioni (CNIT), 43124 Parma, Italy (e-mail: martina.bevacqua@unirc.it; tommaso.isernia@unirc.it).

Joe LoVetri is with the Department of Electrical and Computer Engineering, University of Manitoba, Winnipeg, MB R3T 2N2, Canada (e-mail: joe.lovetri@umanitoba.ca).

Vito Pascazio is with the Centro Direzionale di Napoli, Department of Engineering, University of Naples Parthenope, 80143 Naples, Italy, and also with the Consorzio Nazionale Interuniversitario per le Telecomunicazioni (CNIT), 43124 Parma, Italy (e-mail: vito.pascazio@uniparthenope.it).

Digital Object Identifier 10.1109/TMI.2024.3354463

I. Introduction

KNOWLEDGE of the electromagnetic properties (EPs) of biological tissues, *i.e.* the relative permittivity ε_r and the electrical conductivity σ, is useful in several biomedical applications [1], [2], [3], [4], [5], [6], [7]. The EPs can be related to the typology and physio-pathological status of biological tissues [8], [9]. Indeed, as the EPs of malignant tissues can differ from those of normal tissues, they can play the role of diagnostic biomarkers.

The estimation of *in-vivo* EPs is also relevant in hyperthermia treatment planning, design of electromagnetic medical implants, dosimetry, safety and shimming in magnetic resonance imaging (MRI) scanners [1], [2], [3], [4], [5]. Indeed, in the above medical applications, one needs an accurate knowledge of the field distribution within the region of the body being treated or imaged and the field distribution is directly dependent on the spatial distribution of the EPs. As measurements within the region are usually not possible, the field evaluation relies on numerical simulations, requiring accurate knowledge of the EPs distribution.

Several databases have been reported in the literature that collect the EPs of biological tissues, usually arising from measurements of *ex-vivo* tissue samples, with limitations on inter-subject variability. An example is the IT'IS database [10]. However, according to some studies a non-negligible difference can exist between *ex-vivo* and *in-vivo* EPs. In particular, based on the results in [11], [12], [13], [14], and [15], the *ex-vivo* EPs could differ from the actual *in-vivo* EPs up to 25% for permittivity and 30% for conductivity. Moreover, in [16], [17], and [18] it is observed that the dehydration fraction plays a key role in the measurement of the tissue EPs, so changes between *in-vivo* and *ex-vivo* dielectric properties can be attributed to tissue hydration.

Thus, there is a need for gaining a fundamental understanding of the EPs of tissues and for a non-invasive imaging

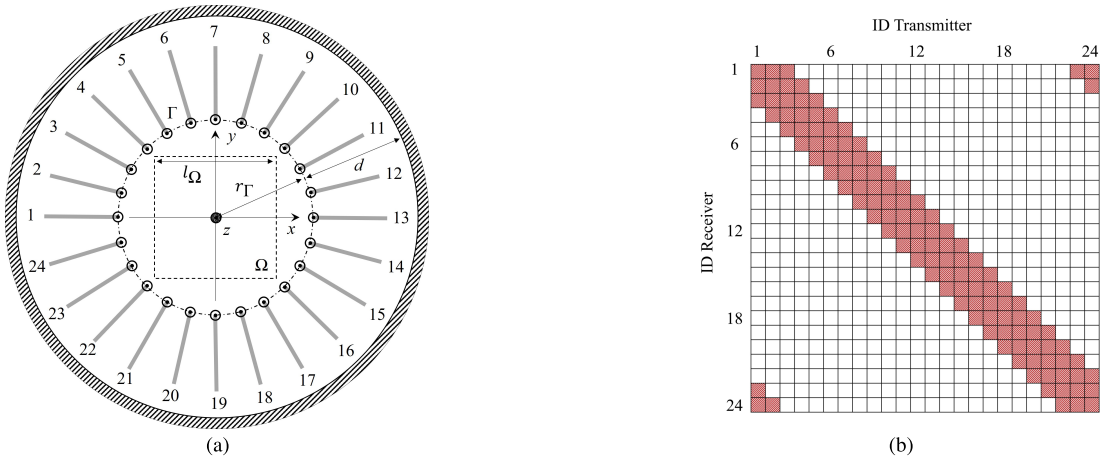

Fig. 1. Sketches of the experimental microwave imaging prototype (a) proposed in [28] and of the measured data arrangement (b). In (b) the red pairs refer to disregarded signals due to direct coupling issues.

modality to obtain the *in-vivo* (subject-specific) estimation of their value. Moreover, according to the precision medicine, there is also the need to investigate and to consider in medical applications the natural human body variability, that is the fact that different individuals can exhibit different EPs for the same tissue [19].

There are several research efforts attempting to non-invasively image the EPs of the biological tissues: electrical impedance tomography [20], magnetic induction tomography [21], magnetic resonance electrical impedance tomography [22] and magnetic resonance based electrical properties tomography [23], just to cite a few. Due to its use of non-ionizing radiation and its potential implementation using relatively inexpensive and portable devices, quantitative microwave tomography (MWT) has gained increasing interest for its use in EPs tomography with respect to other medical imaging techniques [1], [9]. However, MWT exhibits a low spatial resolution and involves the solution of an inverse scattering problem, which is both non-linear and ill-posed [24], [25], [26], [27].

In this respect, the paper has at least two interesting elements of innovation. First, it introduces a new effective three-step method in order to arrive at an accurate and a stable reconstruction of the EPs. Second, by virtue of the above, it improves the fundamental knowledge about tissue properties, contributing to an open debate about the differences between ex-vivo and in-vivo EPs. Results of using quantitative MWT for the extraction of the *in-vivo* EPs of human limbs are provided by processing the data from different human volunteers, with varying ages and levels of adipose tissue, collected by the MWT system developed by the Electromagnetic Imaging Laboratory at University of Manitoba (UofM) [28] working at the frequency range is [0.8,1.2] GHz. More specifically, a novel MWT workflow is introduced that consists in the consecutive construction of three EP images of improved accuracy and resolution from the same collected microwave data. This stepwise procedure creates images with progressively increasing information, starting with segmentations of anatomical regions containing only qualitative information of the EPs and culminating in fully quantitative EP images. By improving the accuracy of the final images and reducing the reconstruction artifacts contained therein (compared to more traditional single-step imaging methods), this workflow provides a much-improved specificity for the imaged tissues.

The paper is organized as follows. In Section II, the basic mathematical formulation of the inverse scattering problem underlying MWT is reported. In Section III, the data set collected using the MWT at the University of Manitoba is briefly described. Sections IV-VII provide details of the proposed quantitative three-step procedure with some simulated and experimental results reported and discussed in Sections VIII and IX. Discussions and conclusions are stated in Sections X and XI.

II. Formulation of the Inverse Scattering Problem

The canonical two-dimensional (2D) scalar field problem with transverse magnetic (TM) polarized fields is considered. A time-harmonic field problem using the $e^{j\omega t}$ time-dependence is assumed and dropped.[1] The 2D TM assumption has been shown to be a relatively good approximation for human forearm imaging [28]. Moreover, line sources can be considered to model the actual dipole antennas used to collect the data.

The inverse problem consists of reconstructing the complex-valued equivalent relative permittivity $\varepsilon_r\left(\underline{r}\right)$, in an imaging domain $\Omega \subseteq \mathbb{R}^2$ that accounts for both the dielectric response as well as the conductivity. The background relative permittivity is denoted by ε_b (it can be a complex quantity, as described in the next section for the data at hand). Then, the contrast function encodes the target properties and is defined as $\chi\left(\underline{r}\right) = \frac{\varepsilon_r\left(\underline{r}\right)-\varepsilon_b}{\varepsilon_b}$. All materials are assumed non-magnetic.

A schematic of the mathematical setup corresponding to the UofM system, described in [28], is depicted in Fig. 1 (see also Section III for more details). N_R receivers and N_T transmitters are located on the measurement line Γ that uniformly encircles the imaging domain. To represent the unknowns, a rectangle of $N_p = N_x \times N_y$ pixels over Ω is considered. With this

[1]The symbol "j" denotes the imaginary unit.

formulation, a discrete version of the scattering equations can be obtained [29]:

$$\boldsymbol{e}_{tot} - \boldsymbol{e}_{inc} = \boldsymbol{A}_i \left(\boldsymbol{x} \odot \boldsymbol{e}_{tot}\right), \tag{1}$$

$$\boldsymbol{e}_{sct} = \boldsymbol{A}_e \left(\boldsymbol{x} \odot \boldsymbol{e}_{tot}\right). \tag{2}$$

In these equations $\boldsymbol{x} \in \mathbb{C}^{N_p \times 1}$ represents the unknown complex-valued contrast vector, $\boldsymbol{e}_{inc}, \boldsymbol{e}_{tot} \in \mathbb{C}^{N_p \times N_T}$ are the vectors which sample the incident and total fields over Ω, and $\boldsymbol{e}_{sct} \in \mathbb{C}^{N_R \times N_T}$ holds the measured scattered field collected for each transmitter-receiver pair. The operator "$\odot$" refers to the Hadamard product (*i.e.*, element-wise product in Ω for each transmitter), while $\boldsymbol{A}_i$ and $\boldsymbol{A}_e$ are the complex matrices that represent the discrete version of the integral scattering operators [30], [31]. The two integral operators are defined on X × T, with X $\subset L^{\infty}(\Omega)$ the subspace of the possible contrast functions, T $\subset L^2(\Omega)$ a proper subspace for the total electric fields inside the object, and with value on two proper subspaces for the scattered field inside and outside the object, $S_e \subset L^2(\Gamma)$ and $S_i \subset L^2(\Omega)$, respectively. The kernel of these operators is the Green's function pertaining to the background medium [29].

Eqs. (1)-(2) incorporate the case of multiple incident views, which allows for the collection of more data in a configuration known as "multiview-multistatic" (MVMS). Thus, to retrieve the geometrical and electromagnetic features of the targets located in the imaging domain, the solution of both Eqs. (1) and (2) is required to determine the contrast function $\boldsymbol{x}$, and thus the complex-valued permittivity, from the collection of the scattering field samples $\boldsymbol{e}_{sct}$. It is well known that finding a solution to such an inverse problem is not trivial because it is nonlinear and ill-posed [26], [27]. Thus, some approximations and proper regularization strategies must be adopted to mitigate these issues with the aim of obtaining more stable and reliable recoveries.

It is well-known that blind inversion, *i.e.*, without supplying the inversion with prior information about the target, typically produces poor results that contain many reconstruction artefacts. On the other hand, incorporating prior information can significantly improve the imaging performance [32], [33].

III. Data Set Description

The UofM data set is composed of both adult male and female forearms whose ages are between 30 and 48 [28]. The selected volunteers are characterized by different percentages of subcutaneous adipose tissues, which allows us to test the imaging capability of the new MWT framework for a wide range of tissue scenarios.

The data was collected using an in-house MWT prototype that is composed of 24 dipole antennas with a quarter wavelength balun that surround the investigation area, as shown in Figure 1(a). The antennas are equally spaced and located on a circle of radius 9.4 cm from the center of the chamber and at mid-height of the cylindrical imaging chamber having metallic walls. The effective operating frequencies range from 0.8 to 1.2 GHz and data was collected by using 0.1 GHz steps. Further details regarding this system and the experimental acquisition protocol can be found in [34] and [35].

For each volunteer, measurement data are available for the arm submerged in several matching fluids of deionized water having different concentrations of table salt. For the results presented in this paper, the matching medium with a concentration of salt of approximately 3.1 grams/liter has been adopted. The presence of salt in the immersion medium introduces losses that reduce the modelling error in the computational inversion model. The relative permittivity of the adopted matching medium in the frequency range of [0.8, 1.2] GHz is approximated as a constant of 77, while its electric conductivity is taken to vary in the range of [0.72, 0.93] S/m. This amount of loss has been shown to effectively mitigate the modelling error incurred by *i*) assuming a 2D TM approximation, and *ii*) ignoring the metallic walls of the chamber and assuming an unbounded medium, i.e. to reduce the mismatch between the assumed computational model (unbounded, 2D homogeneous matching medium) and the physical experiment. Indeed, the reflections from the metallic chamber are significantly attenuated in case of losses in the immersion medium and one is allowed to neglect the presence of the metallic chamber [28]. On the other hand, if the metallic chamber is considered, the Green's function must be substituted with the one pertaining to the enclosed chamber, which can be found numerically, but adds to the complexity of the adopted scattering model.

For each volunteer, 19×24 single-frequency data points (S-parameter measurements) were collected without considering the monostatic contribution and disregarding the signals collected by the four antennas closest to the transmitter position, which can be contaminated by the direct coupling. The overall data organization is reported and sketched in Figure 1(b). The experimental scattered-field data to be inverted for each volunteer was obtained by first subtracting the measurements obtained for the empty fluid-filled chamber (representing the incident field) from the total-field measurements and then calibrated using a calibration coefficient. The calibration coefficient is obtained by taking the ratio of the modelled to measured scattered-field for a 8.89 cm diameter metallic cylinder. Details regarding this procedure can be found in [34] and [36].

IV. The Proposed Multi-Step Microwave Tomography Approach

An overview of the proposed approach is illustrated in Figure 2. More specifically, qualitative images are first generated from the scattered-field data using qualitative inverse scattering techniques [37]. Then, a novel segmentation procedure is used that attempts to introduce an average value for the EPs within the segmented regions. These low-resolution quantitative images are introduced as starting guess within a multi-frequency distorted Born iterative method (DBIM) [38], [39].

In particular, in the first step, qualitative imaging techniques such as the Linear Sampling Method (LSM) [40], the Orthogonality Sampling Method (OSM) [41], Boundary retrieval through Inverse source and Sparsity (BIS) [42] and the Born Approximation (BA) [43], [44], [45] are applied to single-frequency experimental data and compared in

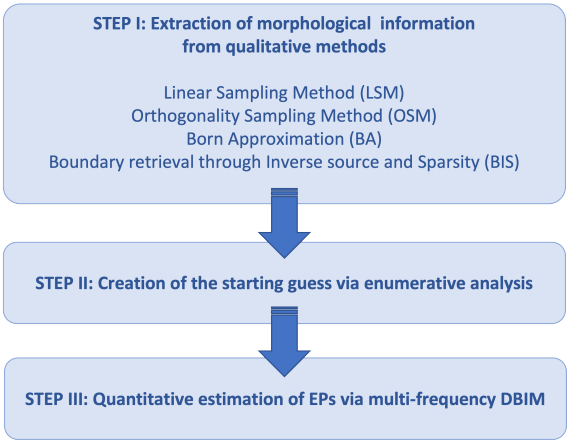

Fig. 2. Scheme of the proposed three-step inversion procedure.

order to extract morphological information of the anatomical region under investigation. Then, in the second step, the obtained qualitative maps are combined and processed, and the Distorted Born Approximation[2] (DBA) [45] inversion is performed to create a low-resolution quantitative image. In the third step, the latter is used as an initial guess for the final quantitative estimation of the EPs.

The detailed explanation of each single step is reported in the following three Sections.

V. Step I: Extraction of Morphological Information From Qualitative Methods

The aim of the first step is to acquire a preliminary understanding of the unknown target within the imaging domain from the data. For this purpose, qualitative methods [37] are adopted as they offer the advantages of solving a simplified problem or an auxiliary linear one, with the absence of false solutions and a negligible computational burden. In fact, they can be exploited to gain preliminary understanding of shape and/or other characteristics of the unknown objects. Moreover, they overcome the limitations of linearized methods and the difficulties related to non-linear optimization while still allowing one to deal with a limited computational burden [37].

In the following, we considered two "sampling" methods that are the LSM and the OSM [40], [41]. The idea underlying LSM and OSM is based on sampling the investigation domain in an arbitrary grid of points and computing in each point an indicator function whose energy will assume different values depending on whether the sampled point belongs or not to the scatterer. To this end, the LSM indicator function is computed by solving an auxiliary linear but ill-posed problem, while the OSM does not explicitly require the solution of a linear problem, as the indicator function is just related to the evaluation of a scalar product. The equation underlying the LSM is the far field equation and in the following it is solved by using the Tikhonov regularization [40]. On the other hand, in the case of far field zone, the OSM is simply the scalar product between the Green's function and the scattered data. Interestingly, OSM has been proven to be able to identify different contrast regions within inhomogeneous targets [46].

As far as the BIS method is concerned, it takes advantage from recent results in the area of sparsity promoting techniques and, provided some conditions hold true, it can retrieve the boundary of unknown targets (rather than their support). Such a method exploits the so-called joint sparsity [47] of the induced currents in the case of perfect electric conductors, and of the equivalent currents in the case of dielectric objects. It is based on the solution of a constrained convex problem, whose objective function to be minimized involves the l_1 norm. As such, it has a higher computational burden compared to LSM and OSM. On the other hand, it does not require the definition of a threshold to identify the target support.

The Born approximation [43], [44], [45] was also used as a first step to gain a preliminary understanding of the shape or other characteristics of the unknown objects. In fact, even when used beyond its range of validity,[3] it can usually recover some useful preliminary information about the shape and location of the scatterer.

In processing the calibrated forearm data, no prior information related to the position or boundaries of the forearm is assumed. Moreover, a square of side-length $l_\Omega = 12$ cm was assumed as the imaging domain, discretized in 120×120 cells. Only for the BIS method, the domain was discretized in 40×40 cells (to reduce the computational burden), while an error on the data equation lower than 30% was permitted (see [42]). The antennas were modelled as filamentary currents located on a circumference of radius $r_\Gamma = 9.4$ cm and embedded in a homogeneous medium with electromagnetic properties of the deionized water and salt. The infinite-domain 2D Green's function for a lossy medium was used in the scattering operators. For this first step of the workflow the working frequency was fixed to 1 GHz, which is the center of the considered bandwidth.

Figures 3-5 report the results for three volunteers, referred as A, B and C, respectively. As can be seen, LSM, BA, BIS and OSM are consistent in identifying the position, the shape, and the size of the relevant forearms. In particular, BIS retrieves the boundary of the limb, while both the OSM and the BA maps allow one to identify the presence of a denser region inside the forearms, for what concerns volunteers A and C. These regions probably correspond to the bones, the Ulna and the Radius. Instead, in the case of volunteer B, some ambiguities are present in the two maps, and one cannot identify the position of bones.

To provides a baseline as reference for the anatomy of each considered volunteer, an MRI image of each forearm is also shown, obtained with a 0.2 T Esaote E-scan XQ (T1 gradient echo protocol). The MRI scans were taken at the same time of the MWT scans and are part of the original experimental dataset. It is worth noting that the MRI and MWT images reported in Figures 3-5 are not co-registered, even though the axes are the same. The accuracy of the co-registration is limited since the volunteer's arm and body positions were

[2]The distorted Born approximation is BA applied in case of inhomogeneous background.

[3]BA holds true in case of scatterers with weak electromagnetic contrast and small dimension in terms of the wavelength.

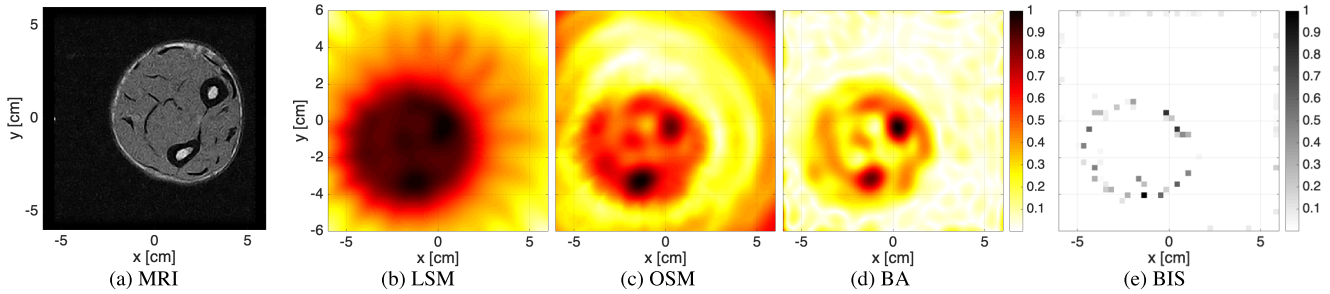

Fig. 3. Volunteer A. T1-weighted MRI image (a). Normalized support indicators at 1GHz obtained via LSM (b), OSM (c), BA (d) and BIS (e). The maximum thickness of the adipose tissue is 3.9 mm [28].

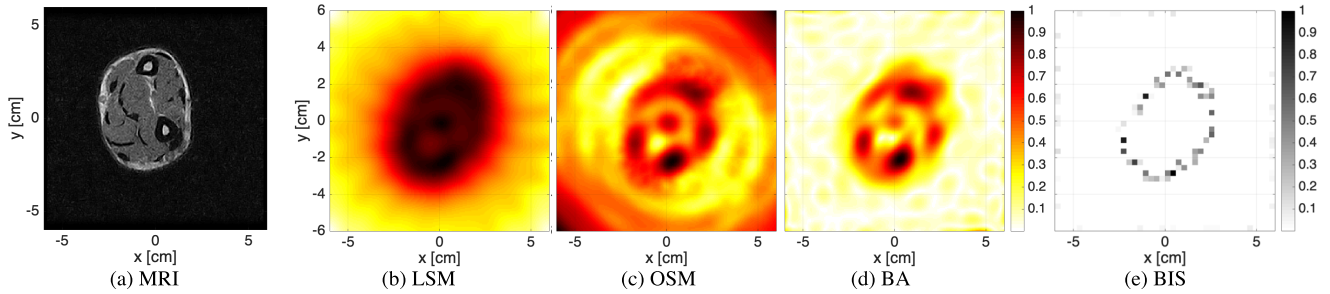

Fig. 4. Volunteer B. T1-weighted MRI image (a). Normalized support indicators at 1GHz obtained via LSM (b), OSM (c), BA (d) and BIS (e). The maximum thickness of the adipose tissue is 7 mm [28].

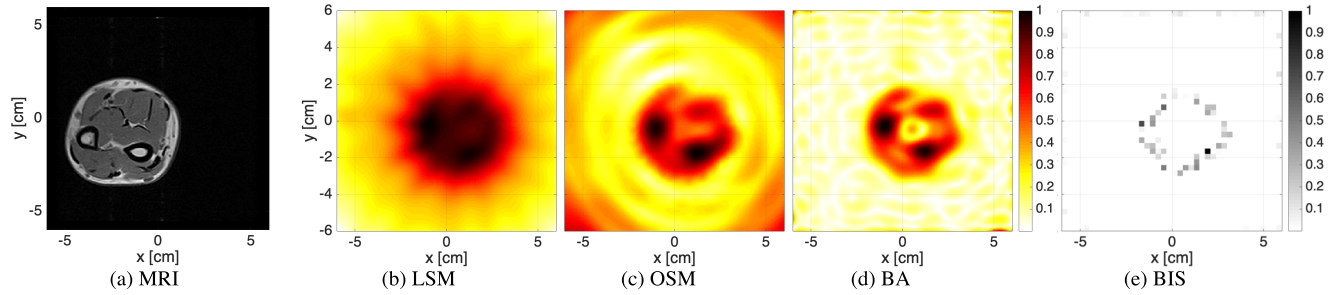

Fig. 5. Volunteer C. T1-weighted MRI image (a). Normalized support indicators at 1GHz obtained via LSM (b), OSM (c), BA (d) and BIS (e). The maximum thickness of the adipose tissue is 4.3 mm [28].

different in the MRI and MWT systems. In the former, the volunteer was supine, and arm held horizontally, while in the latter case the arm was held vertically with the hand clenched in a fist resting on a pad at the bottom of the chamber.

VI. Step II: Creation of the Starting Guess

To improve the qualitative images resulting from Step I and create a suitable initial guess for the multi-frequency quantitative inversion, the morphological information from the LSM map was exploited to identify shape and internal inhomogeneities. In fact, the other qualitative recoveries showed in Figures 3-5 can be richer in terms of morphological information, but these approaches are less stable. For instance, while for volunteers A and C, the OSM and the BA methods can retrieve the bone, in case of volunteer B, both OSM and BA maps exhibit some artifacts which cannot be associated to the presence of the bones. Of course, the previous discarded qualitative maps can be used to validate the successive results.

Specifically, to retrieve further information, the so-called distorted Born approximation (DBA) was adopted. It is important to note that DBA is BA applied to the case of a numerical inhomogeneous background, that is, with respect to a reference known or estimated image, and thus it allows one to retrieve some of the contrast variations and improve the estimated reference image.

In the following, some implicit information is included, i.e. the anatomical region under test is assumed to contain adipose tissue, muscle and bone. The presence of the skin was not considered because its thickness is below the resolution limit in the selected frequency range.

To determine the morphological structure of the above tissues composing the forearm, an accurate segmentation procedure and an enumerative analysis was performed, which consists in the generation of different profiles from LSM and DBA qualitative maps, according to the following sub-steps.

II.a) *Generation of trial adipose-muscle profiles*. The normalized LSM maps $\mathfrak{I}_{LSM}$ were labelled according to a set

of threshold intervals as follows: those pixels wherein $t_{f,i} \leq \mathfrak{I}_{LSM} < t_{m,i}$ are labeled "fat"; the pixels wherein $t_{m,i} \leq \mathfrak{I}_{LSM} \leq 1$ are labeled "muscle", while in the other cases a label associated with the background is assigned. Here, the subscript i spans each of 20 equally spaced thresholds $t_{f,i}$ in the range [0.4, 0.7] and a further 20 thresholds $t_{m,i}$ in the range [0.5, 0.8], respectively; thus, a total of 400 combinations for the pair of threshold-interval is obtained.[4]

Then, for each of the 400 combinations, a reference contrast profile $\boldsymbol{x}_{ref,a}$ was created by filling each labeled region with the corresponding *ex vivo* EP, corresponding to muscle and adipose tissue [28]. In particular, the values $\varepsilon_x = 10 - j$ and $\varepsilon_x = 50 - 20j$ were used for adipose tissue and muscle, respectively.

II.b) *Identification of the bone extension*. DBA [45] was performed for each of the 400 segmented reference profiles $\boldsymbol{x}_{ref,a}$. Then, the normalized DBA maps, $\mathfrak{I}_{DBA}$, were thresholded with a further 20 equally spaced thresholds $t_{b,k}$ within the range [0.5, 0.8] to obtain an estimate of the bone region. In those pixels wherein $t_{b,k} < \mathfrak{I}_{DBA} \leq 1$ the label "bone" was associated. Then, the *ex vivo* EP $\varepsilon_x = 12.4 - 3j$ was assigned to this segmented region and superimposed on the profiles $\boldsymbol{x}_{ref,a}$. Thus, 8000 reference profiles $\boldsymbol{x}_{ref,b}$ were generated in total, by means of the above sub-steps 2.a)-2.b), each quantized into four levels, *i.e.*:

$$label = \begin{cases} background, & 0 \leq \mathfrak{I}_{LSM} < t_{f,i} \\ fat, & t_{f,i} \leq \mathfrak{I}_{LSM} < t_{m,i} \\ muscle, & t_{m,i} \leq \mathfrak{I}_{LSM} \leq 1 \\ bone, & t_{b,k} \leq \mathfrak{I}_{DBA} \leq 1 \end{cases} \tag{3}$$

with $t_{b,k} \in [0.5, 0.8]$, $k = 1, \ldots, 20$, and "*label*" referring to the tissue associated with that quantized threshold-interval.

A sketch of the thresholds per each tissue for Volunteer C is reported in Figure 6 for the sake of clarity.

II.c) *Identification of the best starting guess*. For each of the 8000 generated profiles $\boldsymbol{x}_{ref,b}$, a forward problem was solved, and the obtained data were compared with the calibrated experimental data. The profile that generated modelling data having the minimum mean square error with the calibrated data was selected as a starting guess for the following and final quantitative analysis. This was considered the "best" initial guess having the most accurate morphological structure with segmented EPs of the forearm.

The obtained starting guesses are composed of three tissues, and the EPs are approximated with a stepwise constant function. This is a common assumption for instance in the case of therapeutic treatment planning or when field exposure must be quantified. Thus, this step results in an effective EP segmentation, or discrete-level quantitative morphological reconstruction, of the investigated limb.

VII. Step 3: Quantitative Estimation of EPs via Multi-Frequency Inversion

The nonlinearity of inverse scattering problems contributes to the occurrence of so called "false solutions" typically manifesting as reconstruction artifacts [31]. Hence, the exploitation of a suitable starting guess plays a key role in developing accurate and reliable reconstructions of the EPs. Thus, the best profile obtained in Step II is exploited for local minimization strategies to obtain reliable estimates of the *in vivo* dielectric properties of the biological tissues. In particular, a multi-frequency distorted Born iterative method (MF-DBIM) [38], [39] is adopted to perform the quantitative dielectric estimation of tissue properties. The operative frequency band is [0.8, 1.2] GHz with a frequency step of 100 MHz, and an ohmic model for the complex permittivity was adopted:

$$\varepsilon_x\left(\underline{r}, \omega\right) = \varepsilon'_x\left(\underline{r}\right) - j\frac{\sigma_x\left(\underline{r}\right)}{\omega\varepsilon_0}, \tag{4}$$

in which the quantities ε' and σ are considered independent from the frequency in the selected bandwidth and represent the unknown functions to be determined.

This assumption holds true due to the considered bandwidth [28]. It is worth noting that the multi-frequency data adopted for the inversion were processed simultaneously and not in a frequency hopping fashion. This choice allows the use of the multi-frequency information to improve the recovery performance by reducing the impact of the noise on the quality of the retrieved profile.

Concerning the minimization procedure, the general problem dealt with at the step of the DBIM approach can be summarized as:

$$\Delta \boldsymbol{e}_{sct}^{(k-1)} = \boldsymbol{A}_e^{(k-1)}\left(\Delta \boldsymbol{x}^{(k)} \odot \boldsymbol{e}_{bck}^{(k-1)}\right), \tag{5}$$

with $\Delta \boldsymbol{e}_{sct}^{(k-1)} = \boldsymbol{e}_{sct}^{meas} - \boldsymbol{e}_{sct}^{(k-1)}$ being the difference between the measured scattered field and the simulated scattered field at receivers locations at the $(k-1)$-th iteration, $\boldsymbol{A}_e^{(k-1)}$ and $\boldsymbol{e}_{bck}^{(k-1)}$ are respectively the external radiating operator and the background field pertaining to the contrast profile $\boldsymbol{x}^{(k-1)}$. For this study, Eq. (5) is solved by adopting an iterative conjugate-gradient least-square minimization algorithm and by enforcing constraints on the feasible values of permittivity and conductivity (which must be respectively larger than 1 and positive) only within the support identified according to Step II. Further details regarding the implementation of the adopted minimization scheme for the internal loop of the DBIM can

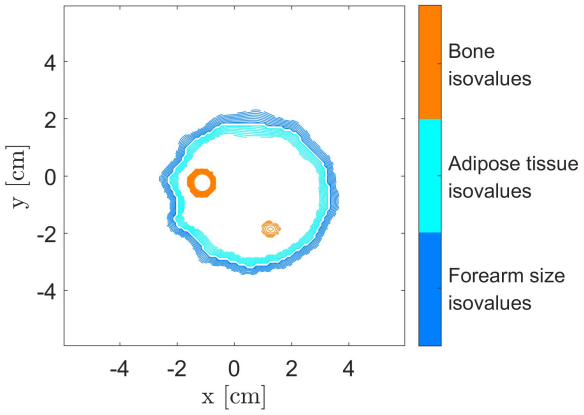

Fig. 6. Iso-value levels for the initial guess generation of Volunteer C, within steps II.a) and II.b).

[4]Despite the ranges are partially overlapped, this does not represent an issue, since any unrealistic profile is automatically discarded within sub-step II.c.

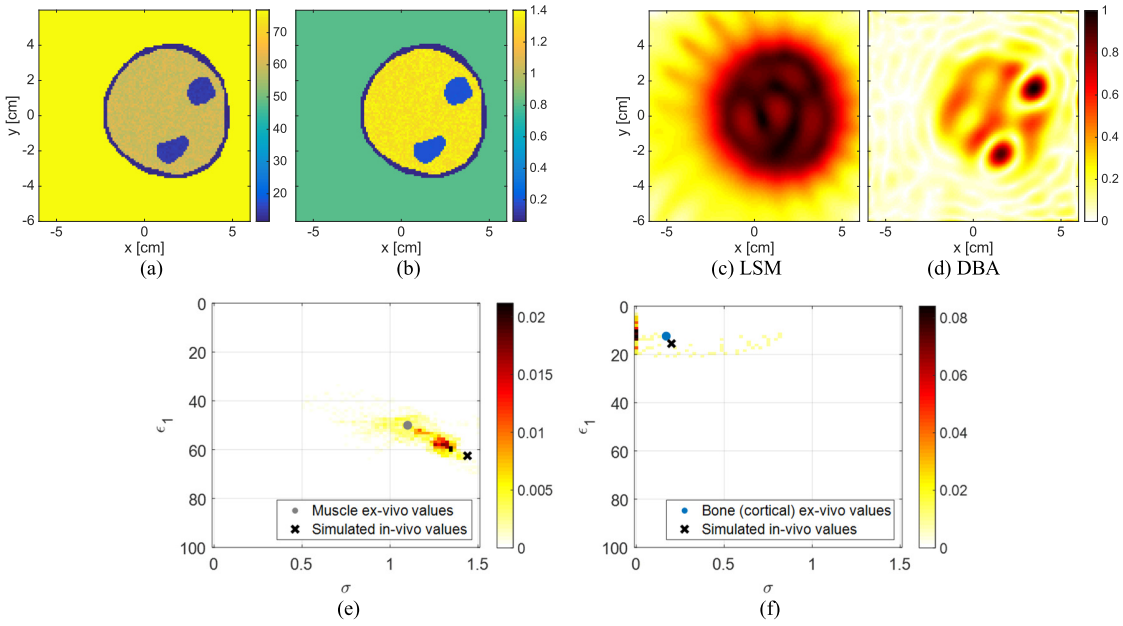

Fig. 7. Test against a 2D simulated scenario: permittivity (a) and conductivity (b) of the reference profile. Normalized support indicators obtained via LSM (c) and DBA (d), and 2D histograms of the retrieved tissue EPs for the muscle (e) and the bone (f).

be found in [48]. At every DBIM step, the variation of the contrast function $\Delta \boldsymbol{x}^{(k)}$ is calculated and used to evaluate the next update as:

$$\boldsymbol{x}^{(k)} = \boldsymbol{x}^{(k-1)} + \Delta \boldsymbol{x}^{(k)}. \tag{6}$$

Furthermore, the inhomogeneous Green's function utilized in the external radiating operator $\boldsymbol{A}_e^{(k-1)}$ as well as the background field $\boldsymbol{e}_{bck}^{(k-1)}$ are updated as well at each iteration of the external loop of the DBIM minimization procedure. That is, at each outer-loop iteration, a new Green's function is numerically evaluated with respect to the updated background, which also includes the updated contrast function. Thus, the electric field related to the new background contrast function (from which the name "background field", $\boldsymbol{e}_{bck}$) is evaluated by means of an in-house method-of-moments forward solver. The previous procedure is repeated until convergence is reached [38], [39], [49], [50], [51]. For the DBIM minimization procedure, a stopping rule is considered by appraising the normalized residual error $NRE_k = \dfrac{\left\| \Delta \boldsymbol{e}_{sct}^{(k-1)} \right\|^2}{\left\| \boldsymbol{e}_{sct}^{meas} \right\|^2}$ at each iteration. If NRE_k is less than 10^{-5}, the procedure is stopped, and $\boldsymbol{x}^{(k)}$ is taken as the solution to the overall problem.

VIII. Numerical Assessment of the Multi-Step Procedure

To assess the accuracy and robustness of the proposed three-step procedure, a 2D numerical simulated test was performed. The 2D scenario aims at mimicking the anatomy of Volunteer A and it is shown in Figure 7 (a)-(b). The working frequency is 1 GHz, the antennas are schematized as filamentary currents rearranged as in the actual experimental MWT system. The data were corrupted with an additive white Gaussian noise with SNR = 30 dB. The numerical phantom has been obtained by segmenting a MRI map of Volunteer A and by associating to each tissue the ex-vivo EPs, but incremented to mimic in-vivo EPs according to [14]. Finally, to deal with a more realistic scenario, the EPs in each voxel of the model have been perturbed by a 10% uniformly-distributed random fluctuation.

Figure 7 (c)-(d) show the qualitative recoveries resulting from step I-II detailed in of Section V-VI, while Figure 7 (e)-(f) report the 2D histograms of the retrieved EPs for bone and muscle tissues. In the 2D histograms, the sum of all bar amplitudes is 1. Moreover, the higher the amplitude associated to a given pair (ϵ, σ) the larger the number of pixels having (ϵ, σ) as EPs.

The results show that the method is able to accurately retrieve the support as well as the true EPs values of the muscle. Indeed, an higher number of pixels have EPs close to the simualted in-vivo value. As far as the bones are concerned, they are correctly detected, but their EPs are not accurately retrieved, probably due to the lower electromagnetic signal penetration, as also discussed in the following Section.

IX. Experimental Results

Figures 8-10 illustrate the retrieved permittivity and conductivity maps for three volunteers obtained by starting the local minimization procedure MF-DBIM from the best initial guess derived in Step II (Figures 8-10 (b),(d)).

As it can be noticed, the quality of the MWI reconstructions is better for those volunteers characterized by a thinner subcutaneous adipose layer (*i.e.*, Volunteers A and C). More specifically, the two volunteers reported in Figures 8 and 10 correspond also to those ones with the highest ratio of the width-to-maximum adipose thickness (similar to the findings reported in [28]). However, it is evident that the amount of subcutaneous adipose tissue strongly impacts on the quality of the recoveries in a negative fashion , *i.e.,* the thicker the adipose layer, the lower the quality of the MWT images.

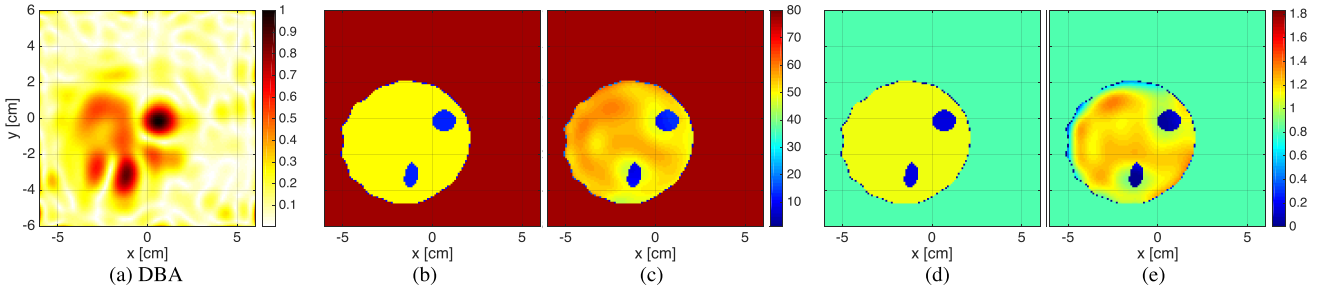

Fig. 8. Volunteer A: normalized DBA indicators at 1 GHz (a). Initial relative permittivity (b) and electric conductivity (d) maps derived from qualitative information (details in Section VI). Retrieved relative permittivity (c) and electric conductivity (e) via MF-DBIM approach.

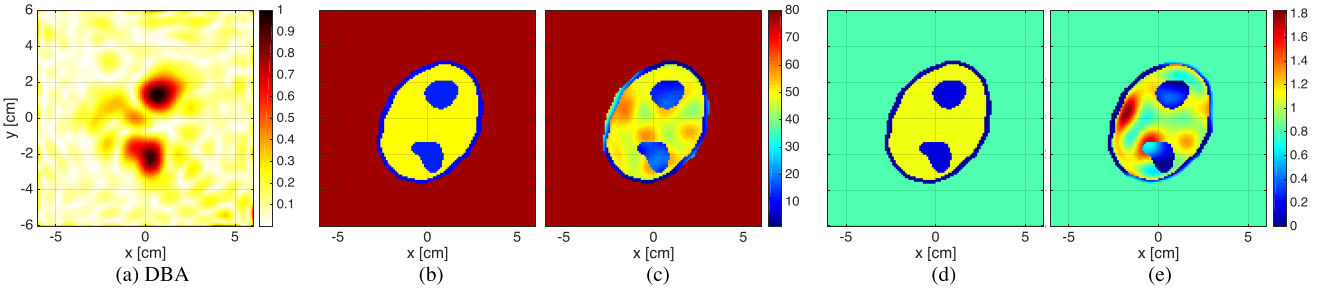

Fig. 9. Volunteer B: normalized DBA indicators at 1 GHz (a). Initial relative permittivity (b) and electric conductivity (d) maps derived from qualitative information (details in Section VI). Retrieved relative permittivity (c) and electric conductivity (e) via MF-DBIM approach.

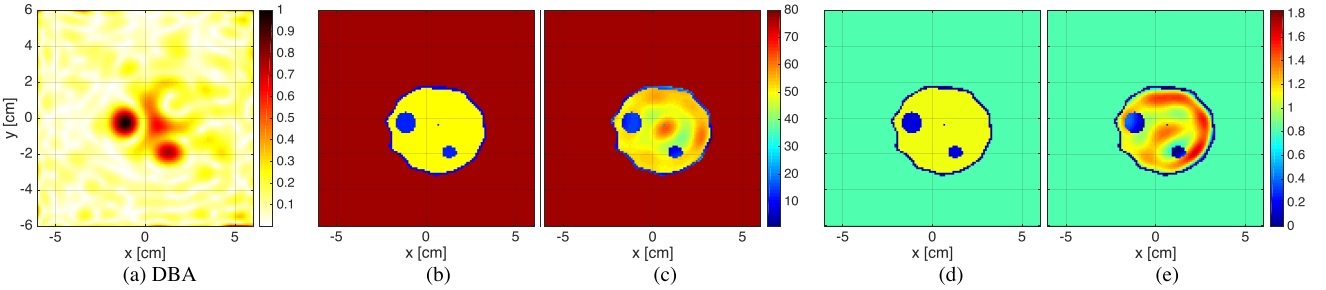

Fig. 10. Volunteer C: normalized DBA indicators at 1 GHz (a). Initial relative permittivity (b) and electric conductivity (d) maps derived from qualitative information (details in Section VI). Retrieved relative permittivity (c) and electric conductivity (e) via MF-DBIM approach.

In the reconstructions, the position and shape of the bone regions and the arms are fully in agreement with results in previous works in [28] and [52]. It is important to note that in [28] the prerequisite morphological information is obtained from initial blind imaging results using manual estimation, while in [52] it is obtained via an ad hoc image segmentation using a simulated annealing technique. Herein, instead, the improved strategy utilizes qualitative reconstructions followed by an accurate tissue-property based segmentation procedure that also considers the bone regions.

Complementary to the maps shown in Figures 8-10, Table I reports the average *in vivo* permittivity and electric conductivity values estimated via this MWT approach for each tissue and volunteer. As confirmed by the previous work [11], [12], [13], [14], [15], [16], [17], [18], several of the *in vivo* tissue EPs are not the same as those measured *ex vivo*. These differences can be due to temperature changes, tissue dehydration, and devascularization of the excised tissues.

To better analyze the quantitative results reported in Figures 8-10, Figure 11 also shows the 2D histograms of the retrieved EPs for each volunteer and tissue. It is worth mentioning that the ex-vivo values reported in Figure 11 refer to the bone tissues that compose the slice of the forearm hosted in the imaging domain (i.e., the cortical and marrow yellow bones).

Despite the spread of the retrieved EPs values, it is possible to notice, also considering the information reported in Table I, that the average values in the muscle are characterized, with respect to their corresponding *ex vivo* values [10], [53], [54], by a slight increment in terms of permittivity and conductivity. This trend is less evident in the case of volunteers with a thicker adipose-tissue layer.

A. Sensitivity Analysis of the Proposed Procedure

Due to the open debate about the difference between ex-vivo and in-vivo dielectric properties, the retrieved values cannot be validated as there is no ground truth for comparison. Moreover, we are retrieving the EPs of three specific human volunteers and, due to the physiological variability of tissues found in the human body, they can be different from the ones of further volunteers. However, in order to somehow validate and

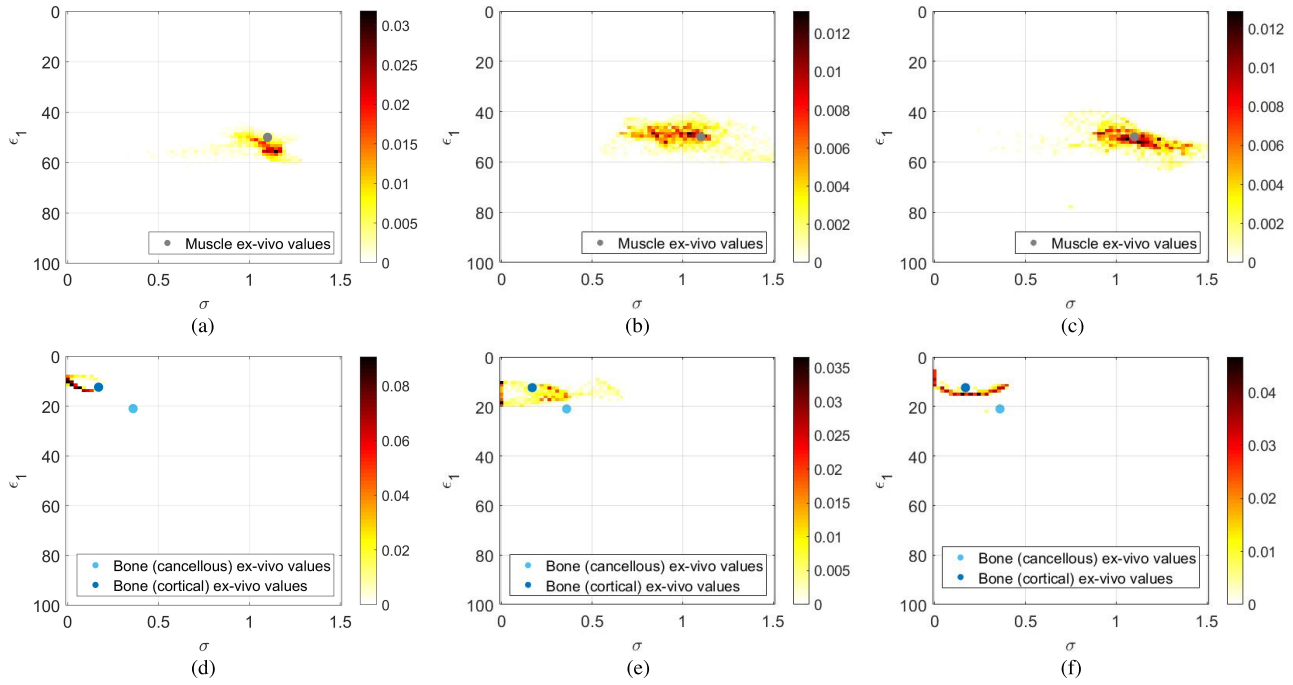

Fig. 11. Two-dimensional histograms of the retrieved permittivity and conductivity values per each volunteer. The recoveries were obtained by means of quantitative multi-frequency inversion (MF-DBIM) as described in Sections VII. Filled circular markers refer to the reference ex-vivo values as reported in [28] per each tissue. (a)-(c): retrieved permittivity and conductivities values in the muscle area defined by the initial guess reported in Figures 8-10(b),(d) at the end of quantitative MF-DBIM inversion for volunteers A, B and C respectively; (d)-(f): retrieved permittivity and conductivities values in the bone area defined by the initial guess reported in Figures 8-10(b),(d) at the end of quantitative MF-DBIM inversion for volunteers A, B and C respectively.

TABLE I
AVERAGE VALUES OF THE IN-VIVO EPS ESTIMATIONS REPORTED IN FIGURES 8-10

TISSUE	RELATIVE PERMITTIVITY			CONDUCTIVITY [S/M]		
	VOLUNTEER			VOLUNTEER		
	A	B	C	A	B	C
MUSCLE	53.5	49.66	51.25	1.12	1.08	1.17
BONE	11.51	15.14	14.54	0.065	0.25	0.24

check the estimated EPs, other articles [28], [35], [55] can be considered wherein the Manitoba dataset was processed.

On the other hand, to test the robustness of the proposed three-step procedure, this subsection presents a sensitivity analysis, which involves the use of different ex-vivo EP values associated to the internal tissues in the enumerative step described in Section VI, in particular steps II.a) and II.b).

The attention is focused on the bone tissue, since a few types exist, each characterized by different EPs (*i.e.*, cancellous, cortical, yellow and red marrow), which are reported in most ex-vivo databases, while only a single type of muscle is usually reported [10]. Due to the in-house microwave acquisition system adopted in this work, the human forearm area under examination is the central part of the long bones "Ulna" and "Radius", also known as "diphysis". The diphysis is the hollow, tubular shaft that runs between the proximal and distal ends of the bone. Inside the diphysis is the medullary cavity, which is filled with yellow marrow bone in the adult. Conversely, the outer walls of the diphysis are composed of dense and hard compact bone, that is the cortical bone [56]. Thus, for the considered case study, it makes sense to consider only these yellow marrow and cortical bone tissues. However, to explore the sensitivity of the proposed approach, all the four different kinds of bone tissue were considered.

For the sake of simplicity and brevity, the proposed sensitivity analysis is shown only for Volunteer A. In particular, Figures 12 and 13 illustrate the corresponding 2D histograms for the bone and muscle tissues, respectively. As can be seen, the muscle tissue does not depend on the choice of the initial ex-vivo parameter of the bone, as confirmed in Figure 13. Thus, the proposed procedure is robust and stable for what concerns the muscle estimation. Conversely, there is a certain dependence on the ex-vivo parameters adopted in step II for the bone tissue. Nevertheless, despite the very different ex-vivo values for the bone, the inversion procedure does not diverge and remains in the range of values characterizing the bone tissue.

X. DISCUSSION

The debate about the difference between ex-vivo and in-vivo dielectric properties is still open. In this respect, the proposed paper aims at contributing to this debate by providing.

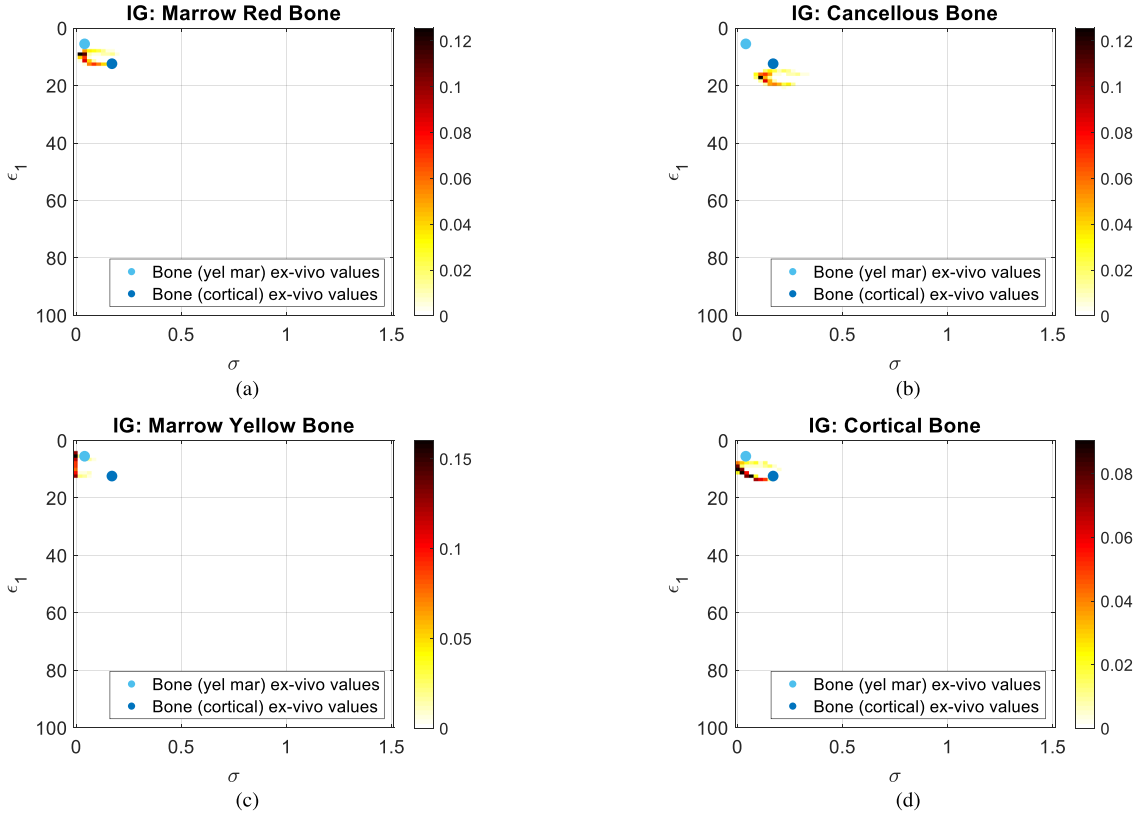

Fig. 12. Two-dimensional histograms of the bone EP values as resulting from the sensitivity analysis with different ex-vivo parameters for the initial guess: (a) marrow red bone, (b) cancellous bone, (c) marrow yellow bone and (d) cortical bone. The legend of the plots shows the ex-vivo values of the two tissues which compose the bone in the imaging region.

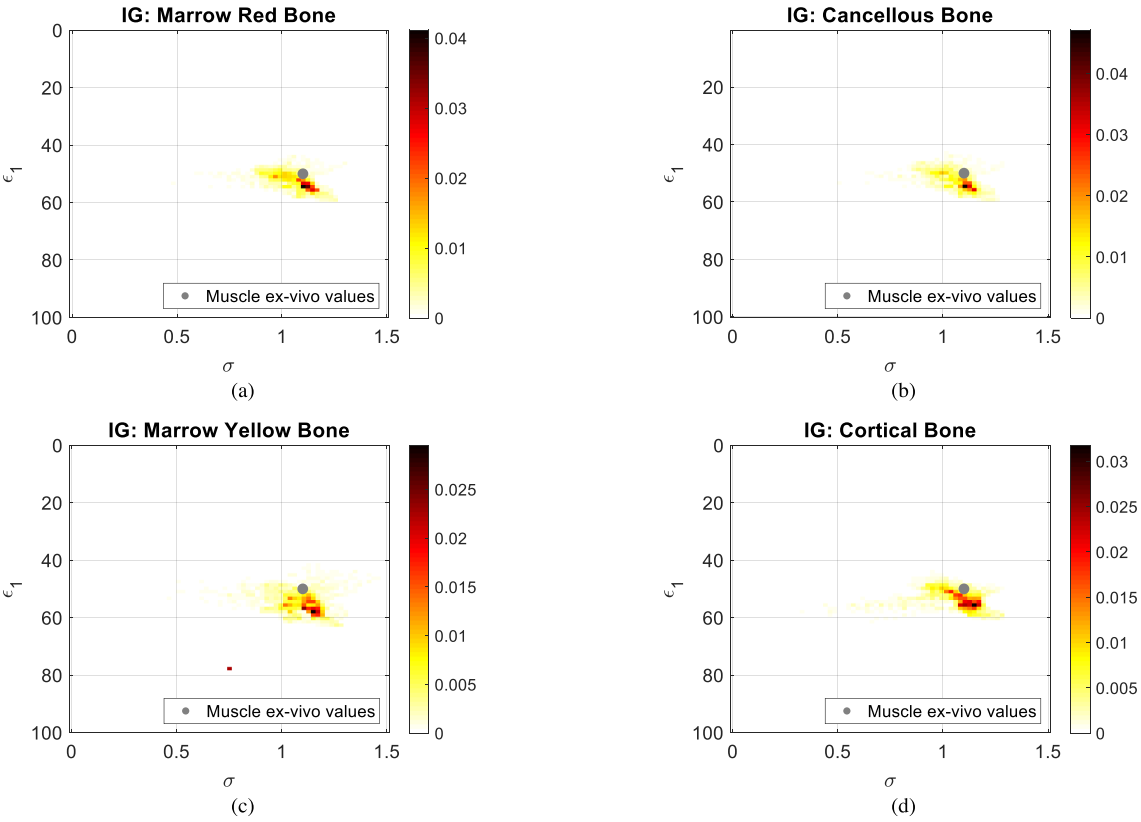

Fig. 13. Two-dimensional histograms of the muscle EP values as resulting from the sensitivity analysis with different ex-vivo parameters for the initial guess: (a) marrow red bone, (b) cancellous bone, (c) marrow yellow bone and (d) cortical bone. The legend of the plots shows the ex-vivo values of the muscle.

Considering the results of Figures 12 and 13, some differences between ex-vivo and in-vivo values can be observed. More in detail, the estimated modal values for the muscle tissue are higher (up to 12% for the relative permittivity and 4% for the electric conductivity) with respect to their corresponding ex-vivo values. Conversely, with respect to the bone tissue, there is not the same stability as with the muscle case. However, these trends seem quite reasonable, as the forearm bones are small structures at the selected operating frequencies (*i.e.*, close to the resolution limits of the imaging system), and surrounded by a lossy, large tissue (*i.e.*, the muscle), that strongly limits the penetration of the electromagnetic signal. Furthermore, the signal propagating inside the muscle, after passing the skin, the subcutaneous adipose layer and the muscle, impinges on the external surface of the bone (the cortical one), that is less dense in terms of EPs with respect to the surrounding tissue, thus contributing to a stronger reflection of the signal with a consequent limitation of its penetration and, therefore, of the quantitative imaging performance. This circumstance is also confirmed by the numerical assessment in Section VIII.

Nevertheless, this analysis highlights one main point of this work, which aims at investigating the potential differences between in-vivo and ex-vivo EPs of biological tissues. As a matter of fact, and observing the results reported in Figure 13, it is possible to see that independently from the choice of the ex-vivo values of the bone in step II, the estimated in-vivo EPs of the muscle look quite stable.

Furthermore, it is worth noting that there is a physiological variability of the biological tissues among the human subjects which further complicate the analysis, as proved by the results reported in Figure 11. Conversely from the case of Volunteer A (Figures 11 (a),(d)), the volunteers characterised by a thicker layer of adipose tissue show a more spread 2D statistical distribution of their tissue EP values, which implies a wider range for both the retrieved relative permittivity and electric conductivity (Figures 11 (b),(c),(e),(f)). By considering also further articles which processed the adopted experimental dataset [28], [35], [55], it is possible to observe that they provide results consistent with the ones presented in this paper. Thus, it is undoubted that the presence of the adipose layer strongly impacts the recovery performance, requiring proper regularization strategies to be adopted in order to obtain more reliable quantitative recoveries of the tissue EPs, such as estimating adipose thickness via proper pre-processing or via alternative strategies, as shown in [28].

An underlying limitation of the proposed analysis is related to unavoidable modelling error introduced by adopting a simplified 2D geometry rather than a 3D one. This assumption neglects the multiple scattering operating among close areas located at different heights. As in previous work, the strategy of adding losses into the matching medium adopted in the experiments can mitigate this limitation, but at the expense of reducing the power of the propagating signal [35].

XI. Conclusion

In this paper, a novel multi-step quantitative MWT approach for the EP retrieval of biological tissues was described. The methodology exploits morphological information derived from single-frequency qualitative inversion steps with the aim of providing a suitable initial guess for multi-frequency quantitative imaging via local minimization procedures.

As a case study, microwave data obtained for the human forearm collected by the Electromagnetic Imaging Laboratory at the University of Manitoba was utilized. The retrieved *in vivo* tissue EPs have been compared with those obtained from the literature using *ex vivo* measurements. Confirming the results of others published in the literature, these values were different, probably due to temperature changes, tissue dehydration, and devascularization as well as the natural variability of tissues found in the human body.

Future work includes the testing of the proposed approach with further volunteers, the improvement of the refinement strategy with better performing quantitative inversions and the more realistic case of three-dimensional geometries. It is important to note that 3D geometry implies a fully vectorial inverse scattering problem and a higher computational burden and memory requirements.

References

[1] N. K. Nikolova, "Microwave imaging for breast cancer," *IEEE Microw. Mag.*, vol. 12, no. 7, pp. 78–94, Dec. 2011.

[2] C. H. Durney, "Electromagnetic dosimetry for models of humans and animals: A review of theoretical and numerical techniques," *Proc. IEEE*, vol. 68, no. 1, pp. 33–40, 1980.

[3] M. de Greef, H. P. Kok, D. Correia, P.-P. Borsboom, A. Bel, and J. Crezee, "Uncertainty in hyperthermia treatment planning: The need for robust system design," *Phys. Med. Biol.*, vol. 56, no. 11, pp. 3233–3250, Jun. 2011.

[4] E. Y. Chow, C.-L. Yang, Y. Ouyang, A. L. Chlebowski, P. P. Irazoqui, and W. J. Chappell, "Wireless powering and the study of RF propagation through ocular tissue for development of implantable sensors," *IEEE Trans. Antennas Propag.*, vol. 59, no. 6, pp. 2379–2387, Jun. 2011.

[5] E. A. Attardo, M. P. Cerquera, F. P. Andriulli, and G. Vecchi, "3-D optimization of magnetic field shimming in MRI by convex programming approach," in *Proc. IEEE Int. Symp. Antennas Propag.*, Jul. 2012, pp. 1–2.

[6] M. Ambrosanio, P. Kosmas, and V. Pascazio, "A multithreshold iterative DBIM-based algorithm for the imaging of heterogeneous breast tissues," *IEEE Trans. Biomed. Eng.*, vol. 66, no. 2, pp. 509–520, Feb. 2019.

[7] D. O. Rodriguez-Duarte, C. Origlia, J. A. T. Vasquez, R. Scapaticci, L. Crocco, and F. Vipiana, "Experimental assessment of real-time brain stroke monitoring via a microwave imaging scanner," *IEEE Open J. Antennas Propag.*, vol. 3, pp. 824–835, 2022.

[8] C. Dachena, A. Fedeli, A. Fanti, M. B. Lodi, M. Pastorino, and A. Randazzo, "Microwave imaging for the diagnosis of cervical diseases: A feasibility analysis," *IEEE J. Electromagn. RF Microw. Med. Biol.*, vol. 5, no. 3, pp. 277–285, Sep. 2021.

[9] R. Chandra, I. Balasingham, H. Zhou, and R. M. Narayanan, "Medical microwave imaging and analysis," in *Medical Image Analysis and Informatics*. Boca Raton, FL, USA: CRC Press, 2017, pp. 451–466.

[10] P. A. Hasgall et al., *Italianist'IS Database for Thermal and Electromagnetic Parameters of Biological Tissues*, document Version 3.0, 2015.

[11] A. J. Wilson, P. Kosmas, and M. Thanou, "Ex-vivo dielectric properties of tissues in athymic nude mice," in *Proc. 3rd URSI Atlantic Asia–Pacific Radio Sci. Meeting (AT-AP-RASC)*, May 2022, pp. 1–4.

[12] R. J. Halter et al., "The correlation of in vivo and ex vivo tissue dielectric properties to validate electromagnetic breast imaging: Initial clinical experience," *Physiol. Meas.*, vol. 30, no. 6, pp. S121–S136, Jun. 2009.

[13] A. P. O'Rourke et al., "Dielectric properties of human normal, malignant and cirrhotic liver tissue: In vivoandex vivomeasurements from 0.5 to 20 GHz using a precision open-ended coaxial probe," *Phys. Med. Biol.*, vol. 52, no. 15, pp. 4707–4719, Aug. 2007.

[14] S. Salahuddin, A. L. Gioia, M. A. Elahi, E. Porter, M. O'Halloran, and A. Shahzad, "Comparison of in-vivo and ex-vivo dielectric properties of biological tissues," in *Proc. Int. Conf. Electromagn. Adv. Appl. (ICEAA)*, Sep. 2017, pp. 582–585.

[15] D. Haemmerich et al., "Changes in electrical resistivity of swine liver after occlusion and postmortem," *Med. Biol. Eng. Comput.*, vol. 40, no. 1, pp. 29–33, Jan. 2002.

[16] D. A. Pollacco, L. Farina, P. S. Wismayer, L. Farrugia, and C. V. Sammut, "Characterization of the dielectric properties of biological tissues and their correlation to tissue hydration," *IEEE Trans. Dielectr. Electr. Insul.*, vol. 25, no. 6, pp. 2191–2197, Dec. 2018.

[17] D. A. Pollacco, L. Farrugia, M. C. Conti, L. Farina, P. S. Wismayer, and C. V. Sammut, "Characterization of the dielectric properties of biological tissues using mixture equations and correlations to different states of hydration," *Biomed. Phys. Eng. Exp.*, vol. 5, no. 3, Mar. 2019, Art. no. 035022.

[18] L. Farrugia, P. S. Wismayer, L. Z. Mangion, and C. V. Sammut, "Accurate in vivo dielectric properties of liver from 500 MHz to 40 GHz and their correlation toex vivomeasurements," *Electromagn. Biol. Med.*, vol. 35, no. 4, pp. 365–373, Oct. 2016.

[19] C. Gabriel and A. Peyman, "Dielectric properties of biological tissues; Variation with age," in *Conn's Handbook of Models for Human Aging*, 2nd ed., J. L. Ram and P. M. Conn, Eds. New York, NY, USA: Academic Press, 2018, ch. 69, pp. 939–952.

[20] Y. Zou and Z. Guo, "A review of electrical impedance techniques for breast cancer detection," *Med. Eng. Phys.*, vol. 25, no. 2, pp. 79–90, Mar. 2003.

[21] H. Griffiths, "Magnetic induction tomography," *Meas. Sci. Technol.*, vol. 12, no. 8, pp. 1126–1131, Aug. 2001.

[22] O. Kwon, E. Je Woo, J.-R. Yoon, and J. Keun Seo, "Magnetic resonance electrical impedance tomography (MREIT): Simulation study of J-substitution algorithm," *IEEE Trans. Biomed. Eng.*, vol. 49, no. 2, pp. 160–167, Feb. 2002.

[23] X. Zhang, J. Liu, and B. He, "Magnetic-Resonance-Based electrical properties tomography: A review," *IEEE Rev. Biomed. Eng.*, vol. 7, pp. 87–96, 2014.

[24] M. Ambrosanio, S. Franceschini, V. Pascazio, and F. Baselice, "An end-to-end deep learning approach for quantitative microwave breast imaging in real-time applications," *Bioengineering*, vol. 9, no. 11, p. 651, Nov. 2022.

[25] X. Chen, *Computational Methods for Electromagnetic Inverse Scattering*. Hoboken, NJ, USA: Wiley, 2018.

[26] M. Bertero and P. Boccacci, *Introduction to Inverse Problems in Imaging*. Bristol, U.K.: Institute of Physics, 1998.

[27] D. Colton and R. Kress, *Inverse Acoustic and Electromagnetic Scattering Theory*. Berlin, Germany: Springer-Verlag, 1998.

[28] C. Gilmore, A. Zakaria, S. Pistorius, and J. LoVetri, "Microwave imaging of human forearms: Pilot study and image enhancement," *Int. J. Biomed. Imag.*, vol. 2013, pp. 1–17, Jan. 2013.

[29] W. C. Chew, *Waves and Fields in Inhomogeneous Media*. Piscataway, NJ, New York: IEEE Publications, 1995.

[30] T. Isernia, V. Pascazio, and R. Pierri, "A nonlinear estimation method in tomographic imaging," *IEEE Trans. Geosci. Remote Sens.*, vol. 35, no. 4, pp. 910–923, Jul. 1997.

[31] T. Isernia, V. Pascazio, and R. Pierri, "On the local minima in a tomographic imaging technique," *IEEE Trans. Geosci. Remote Sens.*, vol. 39, no. 7, pp. 1596–1607, Jul. 2001.

[32] D. Kurrant, A. Baran, J. LoVetri, and E. Fear, "Integrating prior information into microwave tomography part 1: Impact of detail on image quality," *Med. Phys.*, vol. 44, no. 12, pp. 6461–6481, Dec. 2017.

[33] D. Kurrant, E. Fear, A. Baran, and J. Lovetri, "Integrating prior information into microwave tomography part 2: Impact of errors in prior information on microwave tomography image quality," *Med. Phys.*, vol. 44, no. 12, pp. 6482–6503, Dec. 2017.

[34] C. Gilmore et al., "A wideband microwave tomography system with a novel frequency selection procedure," *IEEE Trans. Biomed. Eng.*, vol. 57, no. 4, pp. 894–904, Apr. 2010.

[35] C. Gilmore, A. Zakaria, J. LoVetri, and S. Pistorius, "A study of matching fluid loss in a biomedical microwave tomography system," *Med. Phys.*, vol. 40, no. 2, Jan. 2013, Art. no. 023101.

[36] C. Gilmore, A. Zakaria, P. Mojabi, M. Ostadrahimi, S. Pistorius, and J. L. Vetri, "The university of Manitoba microwave imaging repository: A two-dimensional microwave scattering database for testing inversion and calibration algorithms," *IEEE Antennas Propag. Mag.*, vol. 53, no. 5, pp. 126–133, Oct. 2011.

[37] F. Cakoni and D. Colton, *Qualitative Methods in Inverse Scattering Theory*. Berlin, Germany: Springer-Verlag, 2006.

[38] W. C. Chew and Y. M. Wang, "Reconstruction of two-dimensional permittivity distribution using the distorted born iterative method," *IEEE Trans. Med. Imag.*, vol. 9, no. 2, pp. 218–225, Jun. 1990.

[39] A. J. Hesford and W. C. Chew, "A frequency-domain formulation of the Fréchet derivative to exploit the inherent parallelism of the distorted born iterative method," *Waves Random Complex Media*, vol. 16, no. 4, pp. 495–508, Nov. 2006.

[40] I. Catapano, L. Crocco, and T. Isernia, "OnSimple methodsfor shape reconstruction of unknown scatterers," *IEEE Trans. Antennas Propag.*, vol. 55, no. 5, pp. 1431–1436, May 2007.

[41] R. Potthast, "A study on orthogonality sampling," *Inverse Problems*, vol. 26, no. 7, Jul. 2010, Art. no. 074015.

[42] M. Bevacqua and T. Isernia, "Shape reconstruction via equivalence principles, constrained inverse source problems and sparsity promotion," *Prog. Electromagn. Res.*, vol. 158, pp. 37–48, 2017.

[43] A. J. Devaney, "Geophysical diffraction tomography," *IEEE Trans. Geosci. Remote Sens.*, vol. GRS-22, no. 1, pp. 3–13, Jan. 1984.

[44] M. Ambrosanio and V. Pascazio, "A compressive-sensing-based approach for the detection and characterization of buried objects," *IEEE J. Sel. Topics Appl. Earth Observ. Remote Sens.*, vol. 8, no. 7, pp. 3386–3395, Jul. 2015.

[45] A. G. Tijhuis, K. Belkebir, A. C. S. Litman, and B. P. de Hon, "Theoretical and computational aspects of 2-D inverse profiling," *IEEE Trans. Geosci. Remote Sens.*, vol. 39, no. 6, pp. 1316–1330, Jun. 2001.

[46] M. T. Bevacqua, T. Isernia, R. Palmeri, M. N. Akinci, and L. Crocco, "Physical insight unveils new imaging capabilities of orthogonality sampling method," *IEEE Trans. Antennas Propag.*, vol. 68, no. 5, pp. 4014–4021, May 2020.

[47] M. Fornasier and H. Rauhut, "Recovery algorithms for vector-valued data with joint sparsity constraints," *SIAM J. Numer. Anal.*, vol. 46, no. 2, pp. 577–613, Jan. 2008.

[48] A. Bjõrck, *Numerical Methods for Least Squares Problems*. Philadelphia, PA, USA: Society for Industrial and Applied Mathematics, 1996.

[49] R. F. Remis and P. M. Van den Berg, "On the equivalence of the Newton-Kantorovich and distorted Born methods," *Inverse Problems*, vol. 16, no. 1, p. L1-L4, Feb. 2000.

[50] M. Pastorino, *Microwave Imaging*. Hoboken, NJ, USA: Wiley, 2010.

[51] S. C. Jun and U. Jin Choi, "Convergence analyses of the born iterative method and the distorted born iterative method," *Numer. Funct. Anal. Optim.*, vol. 20, nos. 3–4, pp. 301–316, Jan. 1999.

[52] A. Zakaria, A. Baran, and J. LoVetri, "Estimation and use of prior information in FEM-CSI for biomedical microwave tomography," *IEEE Antennas Wireless Propag. Lett.*, vol. 11, pp. 1606–1609, 2012.

[53] S. Gabriel, R. W. Lau, and C. Gabriel, "The dielectric properties of biological tissues: II. Measurements in the frequency range 10 hz to 20 GHz," *Phys. Med. Biol.*, vol. 41, no. 11, pp. 2251–2269, Nov. 1996.

[54] S. Gabriel, R. W. Lau, and C. Gabriel, "The dielectric properties of biological tissues: III. Parametric models for the dielectric spectrum of tissues," *Phys. Med. Biol.*, vol. 41, no. 11, pp. 2271–2293, Nov. 1996.

[55] M. Ostadrahimi, P. Mojabi, A. Zakaria, J. LoVetri, and L. Shafai, "Enhancement of gauss–newton inversion method for biological tissue imaging," *IEEE Trans. Microw. Theory Techn.*, vol. 61, no. 9, pp. 3424–3434, Sep. 2013.

[56] L. M. Biga et al., *Anatomy & Physiology: OpenStax*. Corvallis, OR, USA: Oregon State University, 2020.

Open Access funding provided by 'Univ Mediterranea di Reggio Calabria' within the CRUI CARE Agreement